Chapter

TROPICAL CYCLONE SIMULATION IN A HIGH-RESOLUTION ATMOSPHERE-OCEAN COUPLED GENERAL CIRCULATION MODEL

Wataru Sasaki[1], Jing-Jia Luo[1,2] and Sebastien Masson[3]

[1]Japan Agency for Marine-Earth Science and Technology, Yokohama, Japan
[2]Centre for Australian Weather and Climate Research, Melbourne, Australia
[3]Laboratoire d'Océanographie Expérimentation et Approches Numériques, Paris, France

ABSTRACT

A global high-resolution coupled general circulation model (CGCM) consisting of a T319 atmosphere general circulation model and an eddy-permitted ocean general circulation model is examined in terms of the reproducibility of the northern hemisphere tropical cyclone (TC) activity as well as the large-scale environmental conditions. The CGCM successfully simulates the realistic TC structure, TC-induced ocean response, and TC genesis frequency. The global TC genesis frequency simulated by the high-resolution CGCM is much closer to the observed, compared that simulated by the medium-resolution (T106) CGCM. In addition, the high-resolution CGCM partially reproduces the bimodal seasonal cycle of the North Indian Ocean cyclogenesis, while the medium-resolution CGCM fails to simulate it. The high-resolution CGCM also reasonably reproduces the environmental conditions favorable for the TC genesis: warm sea surface temperature, low-level cyclonic circulation, weak vertical wind shear, and high relative humidity in the mid-troposphere. The eastward extension of monsoon-trough is well simulated by the high-resolution CGCM as observed, compared to the medium-resolution CGCM. There are, however, still some discrepancies between the modeled and observed TC activity. We discuss about the following two discrepancies from the view point of the simulated large-scale environmental conditions: the high-resolution CGCM fails to reproduce the bimodal seasonal cycle of the Arabian cyclogenesis during the pre-monsoon period, and the western North Pacific TC genesis locations are confined in the southwestern part of the western North Pacific. It is found that less Arabian cyclogenesis during the pre-monsoon period is due to the weak low-level cyclonic circulation in the Arabian Sea during this period, although the weak vertical wind shear is well simulated as observed. For the western North Pacific, less TC genesis in the southeastern part of the

western North Pacific is found to be due to the failure to simulate the eastward extension of the monsoon-trough up to the international dateline. Compared to a medium-resolution CGCM, one of the advantages of the high-resolution CGCM is the reproduction of the intense TC. Surface wind speed exceeding 20~40 ms^{-1} is successfully simulated by the high-resolution CGCM, while the TC wind speed simulated by the medium-resolution CGCM is less than 20~30 ms^{-1}. The frequency distribution of TC surface wind speed simulated by the high-resolution CGCM is closer to the observed compared to the medium-resolution CGCM.

1. INTRODUCTION

Tropical cyclone (TC) is one of the most devastating phenomena in the earth's weather system. The primary driver of the variation of TC activity is large-scale climatic events such as El Nino-Southern Oscillation (ENSO) as well as synoptic events such as Madden-Julian Oscillation [1], and monsoon trough. The modulation of the TC activity and the large-scale climatic events has been extensively studied. Relationship between the western North Pacific TC activity and ENSO was studied by Chan [2] and many scientists. Kim et al. [3, 4] investigated the modulation of the Pacific and Atlantic TC activity by the central Pacific warming, in contrast to the east Pacific warming during the conventional El Nino. The North Atlantic TC activity in relation to the Atlantic Meridional Mode [5] and the North Atlantic Oscillation [6] is also studied. Singh [7] reported the relationship between the North Indian Ocean TC activity and Indian Ocean Dipole mode.

High-resolution atmospheric general circulation models (AGCMs) are necessary for realistic TC simulation and TC forecast. Oouchi et al. [8] discussed possible changes in TC activity under global warming conditions by using a 20-km mesh AGCM. Bengtsson et al. [9] also examined future TC activity in a warmer climate condition by using a high resolution AGCM with T319 (~40km) horizontal resolution.

These high-resolution AGCMs indeed have the capability to realistically simulate TCs. However, the stand-alone AGCMs have limitation due to the lack of the coupled process of the atmosphere-ocean interaction. Importance of atmosphere-ocean coupling for TC simulation was investigated based on regional atmosphere-ocean coupled models. Bender and Ginis [10] pointed out that an uncoupled atmospheric model incorrectly predicts too strong TCs, while a coupled model predicts a cooling of sea surface temperature (SST) associated with the vertical mixing and upwelling which in turn lead to reasonable estimation of the central pressure of TC. Thus the atmosphere-ocean coupling process is indispensable for the realistic simulation of TC intensity.

Atmosphere-ocean coupled model is necessary to reproduce the correct air-sea coupling process in real climate. Coupled general circulation models (CGCMs) have been used to study TC activity on a broad range of time-scales [11-13], although the adopted horizontal resolutions are still too coarse to realistic TC simulation. Vitart and Stockdale [11] reported the occurrence of tropical storms simulated by the ECMWF seasonal forecasting system consisting of an AGCM with T63 horizontal resolution and 31 vertical levels and an ocean general circulation model (OGCM) with $2^{\circ} \times 0.5^{\circ}$ horizontal resolution. Matsuura et al. [12] showed the inter-decadal variability of the western North Pacific TC activity simulated by a medium-resolution CGCM consisting of a T106 AGCM with 19 vertical levels and an

OGCM with $1.125^\circ \times 0.5625^\circ$ horizontal resolution and 37 vertical levels. Iizuka and Matsuura [13] investigated the response of the western North Pacific TC activity to ENSO simulated by a relatively high-resolution CGCM which has an T213 AGCM with 21 vertical levels and an OGCM with $0.5625^\circ \times 0.5625^\circ$ horizontal resolution and 37 vertical levels.

The horizontal resolution of the oceanic component of these CGCMs is coarse to resolve ocean fronts and eddies. Previous study showed that the ocean eddy affects the development of TC intensity [14]. Thus a high-resolution CGCM is expected to realistically simulate the interaction between TCs and ocean fronts and eddies.

In this chapter, a high-resolution CGCM consisting of a T319 (~40km) AGCM and an eddy-permitted OGCM is examined in terms of the reproducibility of the TC activity, particularly in northern hemisphere, as well as the large-scale environmental conditions. As we will show, the high-resolution CGCM realistically reproduces TC structure, TC-induced oceanic response, TC activity, and the large-scale environmental conditions. For comparison, we also examine the performance of a medium-resolution (T106) CGCM in simulating the TC activity.

The rest of this chapter is structured as follows: the CGCMs are introduced in section 2 and we describe the TC detection and tracking method, Sections 3 to 7 presents the TC activity and the large-scale circulation simulated by the high- and medium-resolution CGCMs, and Section 8 provides a summary and discussion.

2. MODEL DESCRIPTION AND TC DETECTION

2.1. The Cgcms and Observed Data

The high-resolution CGCM introduced here is the version 2 of the Scale Interaction Tropical Experiment-Frontier (SINTEX-F2) CGCM, which has been developed from the SINTEX-F1 CGCM [15]. The atmospheric component of the SINTEX-F2 CGCM is ECHAM5 [16] which has T319 horizontal resolution with 31 vertical levels. The model uses a cumulus parameterization scheme proposed by Tiedtke [17]. A 5-layer land surface thermodynamical model is implemented in ECHAM5 [18]. The oceanic component is based on the Nucleus for European Modelling of the Ocean (NEMO) modeling system [19] which includes an ocean model of the Océan Parallélisé (OPA9) and a sea-ice model of the Louvain-la-Neuve Sea Ice Model (LIM2; [20]). The OPA9 and LIM2 employ the ORCA-R025 grid which uses a tri-polar grid with 0.25° zonal resolution and 0.25°cos(latitude) meridional resolution with 46 vertical levels. The atmospheric and oceanic components are coupled with data exchanged every 2 hours, including SST, sea-ice fraction and thickness, water, surface heat, and momentum fluxes, by means of the Ocean Atmosphere Sea Ice Soil (OASIS3) coupler [21] without applying any flux correction. Therefore the feedback of strong surface currents driven by the TC winds on the wind stress forcing has been taken into account. Following Luo et al. [15], the momentum flux of ocean surface current is directly passed to the atmosphere. The model is initialized by setting the temperature and salinity in climatological January equal to the Levitus [22], and a state of the rest without motion. Due to the limited computational resources, the SINTEX-F2 CGCM is integrated for 20 years and the outputs from the model year 6 to year 20 are used for the analysis. We note that the 5-yr

model spin-up is still too short to reach the equilibrium states. In fact, the modeled tropical SST has a positive trend which is greater than that observed during 1980-2008 (not shown). Considering that TC activity is influenced by the SST, further model spin-up is necessary. Therefore our results described in this chapter should be viewed as the preliminary results.

We also use the outputs of the SINTEX-F1 CGCM with a medium resolution. The atmospheric component of the SINTEX-F1 is ECHAM4 [23] which has T106 (~100km) horizontal resolution with 19 vertical levels. The oceanic component is the Océan Parallélisé (OPA8.2; [24]). The OPA8.2 employs the ORCA-R2 grid which uses a tri-polar grid with 2° zonal resolution, and a meridional resolution varying from 0.5° at the equator to 2°cos(latitude) pole-ward of 20° with 31 vertical levels. The atmospheric and oceanic components are coupled with data exchanged every 2 hours by means of the Ocean Atmosphere Sea Ice Soil (OASIS2.4) coupler [25] without applying any flux correction. The initialization method is the same as that used for the SINTEX-F2. The SINTEX-F1 CGCM is integrated for 180 years, and the last 15 years are used for the analysis. Readers are referred to [15] for detailed model descriptions.

We employ observed TC data obtained from the National Hurricane Center and the U.S. Joint Typhoon Warming Center. The TC climatology is calculated from the data during 1980-2008 during which observed data are reliable thanks to an introduction of satellite altimeter measurements. To validate the modeled environmental conditions, we use the 1980-2008 mean of the National Center for Environmental Prediction/National Center for Atmospheric Research (NCEP/NCAR) Reanalysis [26]. We also use HadISST [27] which contains observed SST and global sea ice coverage during 1980-2008.

2.2. Method of TC detection

Many different TC detection and tracking schemes have been proposed [28]. Since TCs are characterized by cyclonic circulation associated with strong low-level winds and the warm-core in the mid-troposphere, the features are reflected in most schemes to detect model TC. However, different detection criteria for the threshold in low-level wind speed, low-level vorticity, and warm-core temperature anomaly are employed in individual schemes respectively. In addition, the lifetime of the TC is taken into consideration.

We employ a TC detection and tracking scheme proposed by Iizuka and Matsuura [13]. The scheme employs the surface wind speed threshold (17 ms^{-1}) and surface vorticity threshold (1.5×10^{-4} s^{-1}). The lifetime is required to be longer than 2 days. To exclude the mid-latitude cyclones, the genesis locations are limited within the 30°S-30°N. In addition to their detection scheme, we impose a limitation on the warm-core temperature anomaly. The sum of temperature anomaly at the 700-, 500-and 300-hPa levels is greater than 1.0 K for the high-resolution CGCM, while it is greater than 0 K for the medium-resolution CGCM. The surface wind speed threshold for the high-resolution CGCM is 17 ms^{-1}, while that is changed to 12 ms^{-1} for the medium-resolution CGCM. Walsh et al. [28] proposed a resolution-dependent TC detection and tracking scheme, and recommended to apply the higher surface wind speed threshold for higher-resolution atmospheric models. From their criteria, the surface wind speed threshold for T319 (~40-km) and T106 (~100-km) AGCM is ~17 ms^{-1} and ~15 ms^{-1}, respectively. Our criteria for the high-resolution CGCM satisfy their criteria,

while our criteria for the medium-resolution CGCM are not stringent as the recommended threshold. As described in Walsh et al. [28], using a lower threshold leads to an artificial increase in the TC genesis frequency in a simulation. Our low surface wind speed threshold (12 ms^{-1}) may artificially increase the TC genesis frequency in the medium-resolution CGCM. Nevertheless, as we will see, the TC genesis frequency in the medium-resolution CGCM is less than those of observation and high-resolution CGCM simulation. Although we have tried some different combination of the threshold values for the relative vorticity and surface wind speed, the relative relationship of the TC genesis frequency between the SINTEX-F1 and SINTEX-F2 is not unduly changed.

3. TROPICAL CYCLONES SIMULATED BY THE HIGH-RESOLUTION CGCM

We briefly describe, by taking as some examples, a TC structure and response of ocean to TCs simulated by the high-resolution CGCM (SINTEX-F2).

In the CGCM, a TC-like vortex occurred at 10.7˚N, 142.9˚E on 07OCT0018. The TC moved northwestward until 12OCT0018, then moved westward and made landfall on Vietnam (the TC track is shown as red line in Figure 1). The westward propagation of the TC is one of the typical TC tracks during boreal autumn in the western North Pacific. The TC reached its peak strength of the central pressure at 956 hPa with the maximum surface wind speed of 39.8 ms^{-1}. Figure 1 shows the horizontal distribution of sea level pressure, precipitation, and surface wind field of the simulated TC at its mature stage. The decrease in sea level pressure associated with the strong low-level cyclonic circulation is well simulated. The heavy rainfall exceeding 20 mm/hr associated with the TC is simulated. Figures 2a and 2b show the vertical section of zonal and meridional winds of the TC, respectively. The cyclonic structure is maintained up to the 200-hPa level. The weak wind speed at the center of the TC is also simulated. The warm-core exceeding 5°C associated with the strong ascent flow (Figure 2c) is simulated. Although the horizontal resolution of the T319 AGCM is still coarse to resolve the finer structure such as eye wall of a TC, overall characteristics of a modeled TC are in reasonable agreement with observations [29].

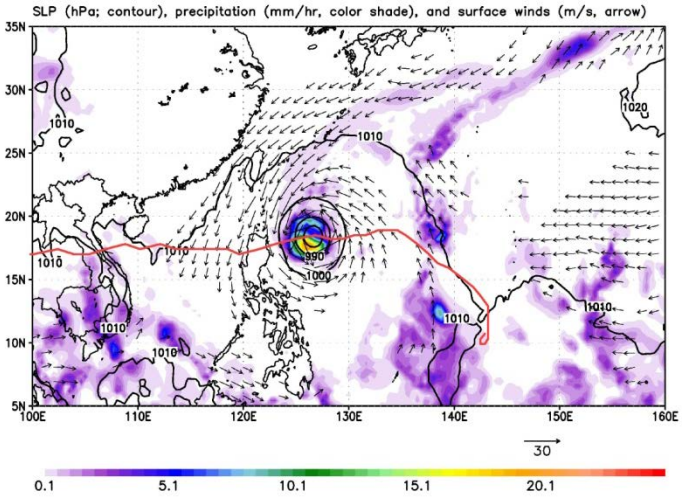

Figure 1. Sea level pressure (contour; hPa), precipitation (color shade; mm hr^{-1}), surface wind vectors (arrow; ms^{-1}) of a TC-like vortex simulated by the SINTEX-F2. The contour interval is 10-hPa. The surface wind vectors are shown for the magnitude exceeding 8 ms^{-1}. Red line denotes the track of the TC.

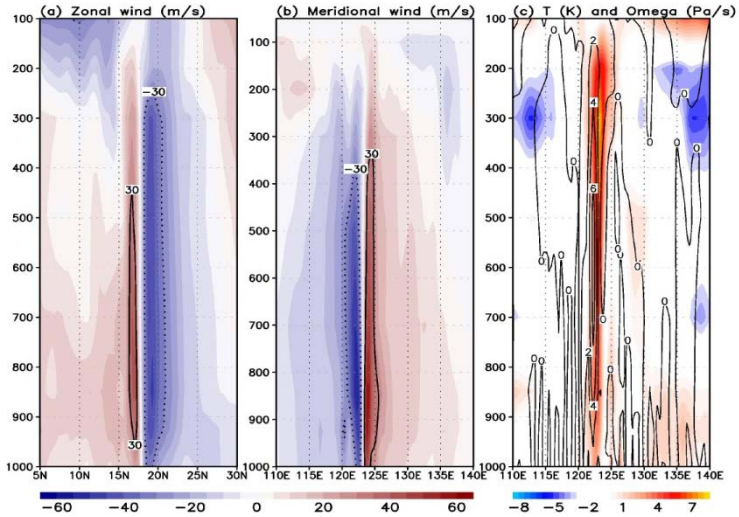

Figure 2. Vertical section of (a) zonal wind (ms^{-1}), (b) meridional wind (ms^{-1}), (c) temperature anomaly (color; K) and vertical wind speed (contour, Pa s^{-1}) associated with a TC in Figure 1. The contour in (a) and (b) shows the wind speed exceeding 30ms^{-1}.

The high-resolution CGCM also simulates the realistic ocean response to a TC passage. The black line in Figure 3a shows a track of a simulated TC which occurred at 7.7˚N, 137.2˚E on 29NOV0019. The TC reached its peak strength of the central pressure at 971.9 hPa, and the surface wind speed was enhanced to 35.6 ms^{-1} at its mature stage. During the passage of the TC, the cyclonically rotating winds (not shown) generated the surface currents which flow nearly the same direction as the surface winds (Figure 3a). Not only the surface currents beneath the TC, but also the strong surface currents behind the TC after the TC passage are

simulated (Figures 3a-e). In this case, SST is not drastically cooled as observed, although observations indicate that the SST cooling induced by TCs ranges from 1˚C to 6˚C [30]. Deep thermocline/mixed layer in the tropical western Pacific may prevent the cooling of SST. Instead, a significant vertical motion in the subsurface induced by the TC is seen in the model. Figures 3e-h show the simulated vertical current velocity during 02DEC0019-05DEC0019. The vertical motion induced by the TC consists of two components: the upwelling associated with the Ekman pumping forced by the surface winds and near-inertial oscillations characterized by a pattern of cells of upwelling and downwelling behind the TC. Figure 3h clearly shows the TC-induced upwelling beneath the TC and the alternate upwelling and downwelling behind the TC. The simulated ocean currents induced by the TC are consistent with the observed and previous modeled results [31, 32].

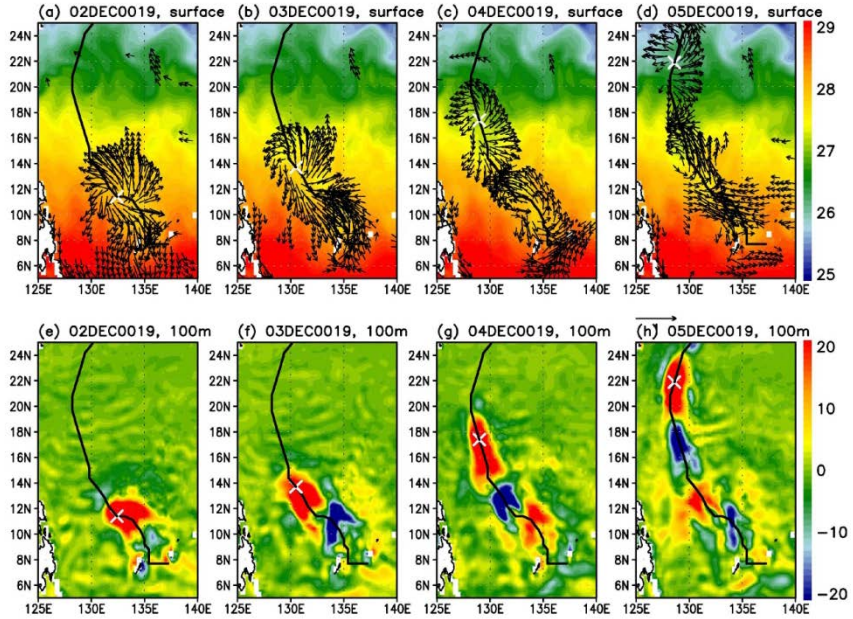

Figure 3. (a-d) SST (color shade; °C) and surface currents (arrow; ms^{-1}) associated with a TC passage during 02DEC0019-05DEC0019 simulated by the SINTEX-F2. The surface current velocity less than 0.2 ms^{-1} is omitted. Bold line denotes the TC track. Cross mark shows the position of the TC. (e-h) As in (a-d), but for the vertical current velocity (color shade; m day^{-1}) at the 100-m depth.

Figure 4 shows changes in SST associated with the passage of a simulated TC in the eastern North Pacific during 10SEP0015-16SEP0015 in the high-resolution CGCM. The SST is reduced by the TC passage particularly on the right hand side of the moving direction (Figures 4a-d). Different from the less SST cooling during the TC passage from 02DEC0019 to 05DEC0019 in the western North Pacific (Figure 3), SST cooling associated with the TC passage during 10SEP0015-16SEP0015 is remarkable. The strong SST cooling could be caused by both the TC passage near the SST front and a shallow thermocline in the eastern North Pacific. On the other hand, Wu et al. [14] showed that the ocean eddy affects the development of TC intensity. These are good examples that a high-resolution CGCM has a capability to simulate the interaction between TCs and ocean fronts and eddies.

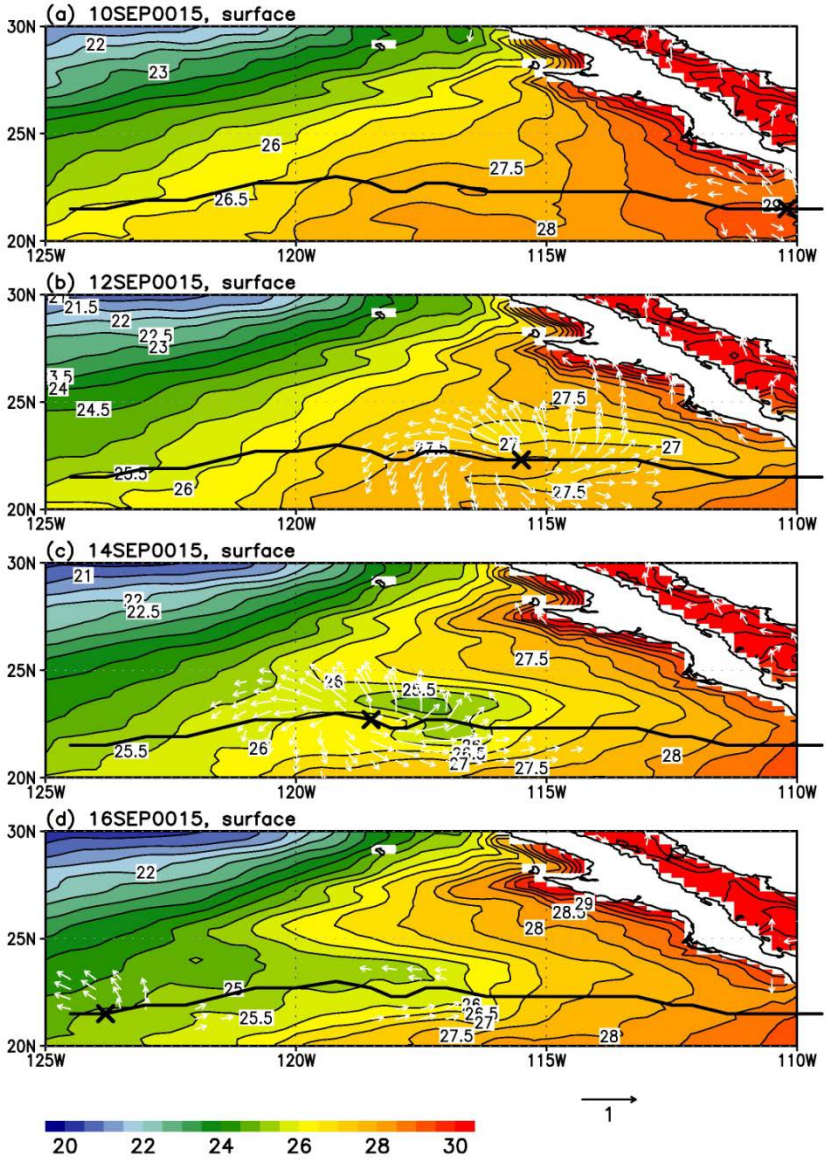

Figure 4. SST (color shade; °C) and surface currents (arrow; ms^{-1}) associated with a TC passage during 10SEP0015-16SEP0015 simulated by the SINTEX-F2. The surface current velocity less than 0.2 ms^{-1} is omitted. Bold line denotes the TC track. Cross mark shows the position of the TC.

Thus, the high-resolution CGCM has a capability to simulate realistically the atmosphere-ocean phenomenon associated with TCs.

4. ENVIRONMENTAL FIELDS SIMULATED BY THE HIGH-RESOLUTION CGCM

Gray [33, 34] showed that warm SST, high vorticity in the low-troposphere, weak vertical wind shear, and high humidity in the mid-troposphere are favorable large-scale conditions for TC genesis. In this section, we evaluate the performance of the high-resolution CGCM in terms of capturing these large-scale environmental conditions.

Figure 5a shows SST averaged for the TC peak season in the northern hemisphere (June-November) simulated by the SINTEX-F2 CGCM. The horizontal distribution of the SST is in general agreement with that observed (Figure 5c). The SST warmer than 26˚C, which is a favorable condition for TC genesis, in the tropical oceans is well simulated as observed (Figure 5a). Meanwhile, the Pacific cold tongue SST in the SINTEX-F2 is approximately 1˚C warmer than the observed (Figure 5a). The warm SST bias may be due to the weak equatorial upwelling associated with the weak easterlies in the model when compared to those observed (Figures 6a and 9.6c). For the tropical Atlantic, the modeled SST to the west of African continent is warmer than that observed (Figure 5a). The warm SST bias in the eastern equatorial Atlantic is one of the common problems for most of current CGCMs [35] to be solved. The medium-resolution CGCM (SINTEX-F1) also generally simulates the SST as observed, although there is a warm SST bias in the North Indian Ocean (Figure 5b).

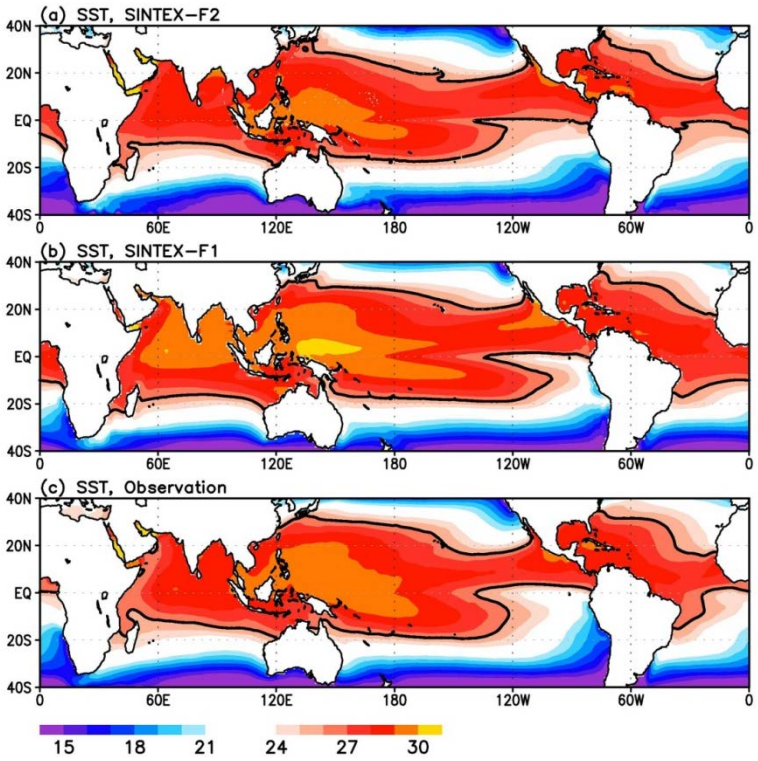

Figure 5. Climatological Jun-November mean of SST (color shade; °C) from the (a) SINTEX-F2, (b) SINTEX-F1, and (c) HadISST. Bold line denotes the 26°C isotherm.

The modeled wind fields at the 850-hPa level also accord with those observed (Figure 6). In particular, the eastward extension of monsoon westerly to the east of the Philippines in the SINTEX-F2 is well simulated as observed (Figures 6a and 9.6c). We however note that the modeled easterly extends slightly westward compared to the observed. On the other hand, the eastward extension of the monsoon westerly in the SINTEX-F1 is weaker than that observed (Figures 6b and 9.6c). The eastward extension of the monsoon-trough is one of the key factors for the western North Pacific cyclogenesis [36]. We further examine the seasonal cycle of the western North Pacific TC genesis frequency and the large-scale circulation simulated by the CGCMs in Section 6.

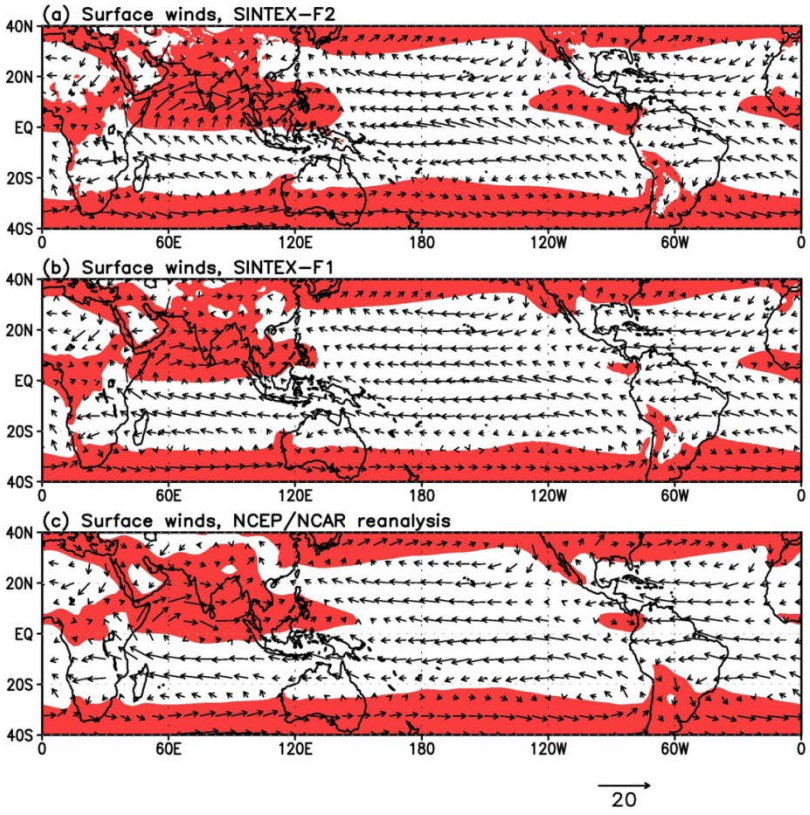

Figure 6. Climatological June-November mean of wind vectors (ms^{-1}) at the 850-hPa level from the (a) SINTEX-F2, (b) SINTEX-F1, and (c) NCEP/NCAR reanalysis. Red denotes the positive zonal surface wind speed.

Figure 7 shows a comparison of the relative vorticity at the 850-hPa level simulated by the CGCMs and that observed. The modeled strong cyclonic circulation in the Arabian Sea, Bay of Bengal, western North Pacific, eastern North Pacific, and tropical North Atlantic is in good agreement with that observed. However, the low-level vorticity in the eastern North Pacific simulated by the SINTEX-F2 extends further northward compared to that observed (Figures 7a and 9.7c).

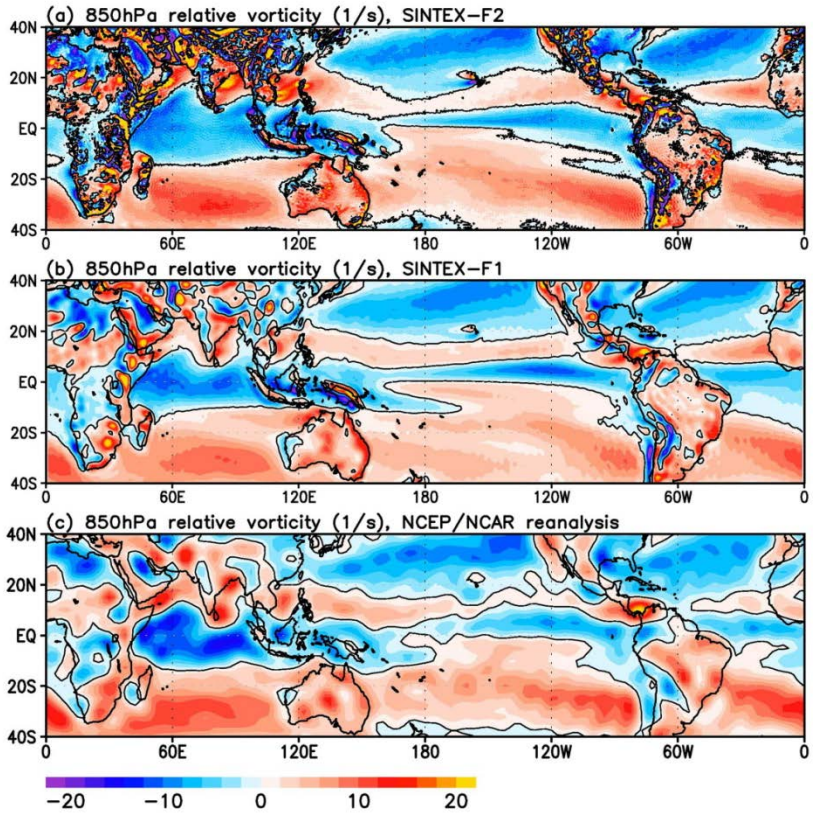

Figure 7. Climatological June-November mean of the relative vorticity at the 850-hPa level (color shade; $\times 10^{-6}$ s^{-1}) from the (a) SINTEX-F2, (b) SINTEX-F1, and (c) NCEP/NCAR reanalysis. The contour denotes the zero line.

The modeled and observed relative humidity in the lower troposphere has a good agreement in the spatial pattern: relatively high humidity in the region of tropical convection and relatively low humidity in the mid-latitudes (Figure 8). However, there is a discrepancy between the modeled and observed relative humidity in the region of tropical convection. The relative humidity at the 700-hPa level in the region of tropical convection simulated by the CGCMs is greater than that of the NCEP/NCAR reanalysis (Figure 8). Trenberth and Guillemot [37] pointed out that the NCEP/NCAR reanalysis has a substantial dry bias in the region of tropical convection associated with the weak Hadley circulation. Annamalai et al. [38] suggested the tendency for the Arakawa-Schubert convection scheme to dry the tropical atmosphere. The difference in the convection scheme between the NCEP/NCAR reanalysis AGCM (Arakawa-Schubert convection scheme) and the CGCMs (Tiedtke convection scheme [17]) may lead the difference in the magnitude of the humidity in the region of tropical convection. The relative humidity simulated by the SINTEX-F2 is much greater than that of the SINTEX-F1 (Figures 8a and 8b). This is consistent with too strong tropical convective precipitation in the SINTEX-F2.

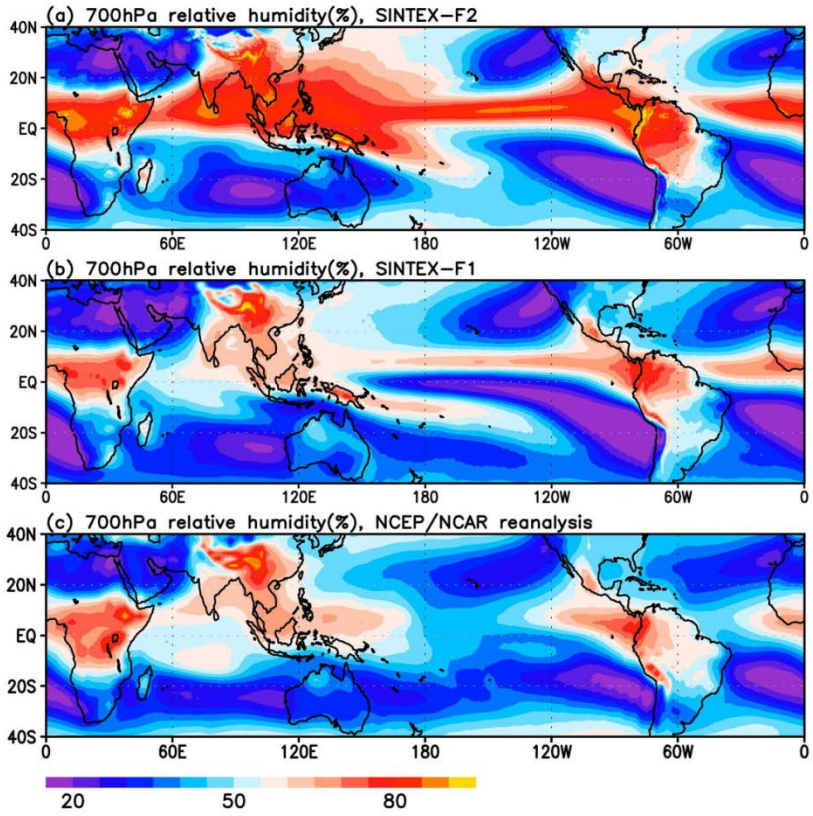

Figure 8. Climatological June-November mean of the relative humidity (%) at the 700-hPa level from the (a) SINTEX-F2, (b) SINTEX-F1, and (c) NCEP/NCAR reanalysis.

Figure 9 shows the climatological June-November mean of the magnitude of the vertical wind shear from the CGCMs and the NCEP/NCAR reanalysis. The simulated vertical wind shear, calculated as the difference of the winds between the 850- and 200-hPa levels, accords with that observed. The vertical wind shear in the eastern North Pacific simulated by the SINTEX-F2 is slightly stronger than that of the SINTEX-F1 (Figures 9a and 9b). This indicates that the eastern North Pacific cyclogenesis in the SINTEX-F2 is less than that of the SINTEX-F1. However, as we will see, the eastern North Pacific cyclogenesis in the SINTEX-F2 is greater than that of the SINTEX-F1 (Table 1). The higher low-level vorticity and mid-level humidity in the SINTEX-F2 relative to the SINTEX-F1 (Figures 7 and 8) may enhance the eastern North Pacific cyclogenesis in the SINTEX-F2.

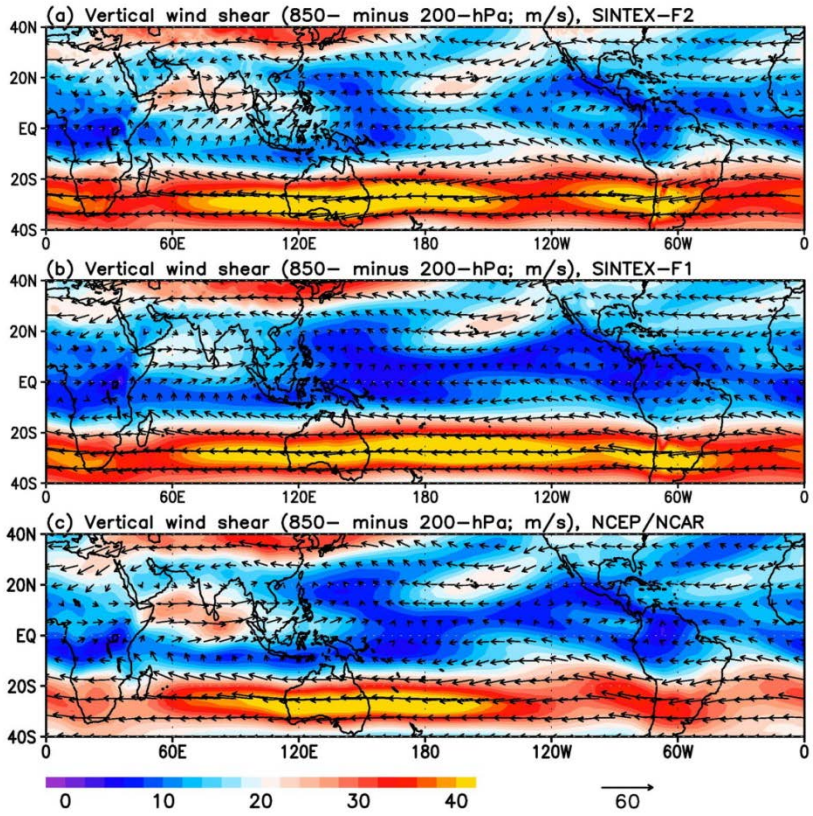

Figure 9. Climatological June-November mean of the magnitude of the vertical wind shear (color shade; ms^{-1}) and vertical wind shear vector (arrow) from the (a) SINTEX-F2, (b) SINTEX-F1, and (c) NCEP/NCAR reanalysis. The vertical wind shear is calculated as the difference in wind speed between the 850- and 200-hPa levels.

Table 1. The annual mean of observed and simulated TC genesis frequency

	Global	Western North Pacific	Eastern North Pacific	North Indian Ocean	North Atlantic
SINTEX-F2	78.0	21.5	15.5	3.7	8.3
SINTEX-F1	46.6	10.3	5.2	2.4	3.5
Observation	81.4	27.6	15.6	4.6	9.6

The vertical wind shear in the North Indian Ocean simulated by the SINTEX-F1 is weaker than that of the SINTEX-F2, indicating that the North Indian TC genesis in the SINTEX-F1 may be greater than that of the SINTEX-F2. We however note that the North Indian cyclogenesis in the SINTEX-F1 is less than that of the SINTEX-F2 (Table 1). The less North Indian cyclogenesis in the SINTEX-F1 may be due to the lower relative vorticity and relative humidity when compared to the SINTEX-F2 (Figures 7 and 8).

5. CLIMATOLOGICAL TC GENESIS FREQUENCY

In this section we examine the reproducibility of the climatological TC genesis frequency simulated by the SINTEX-F2 and SINTEX-F1.

It has been well known that there are four major TC genesis basins in the northern hemisphere: the western North Pacific, eastern North Pacific, North Indian Ocean, and North Atlantic. Table 1 shows the annual mean of the modeled and observed TC genesis frequency over the whole globe as well as the four TC basins. The annual mean of the global TC genesis frequency simulated by the SINTEX-F2 (78) is comparable to that observed (81.4). The regional TC frequency is also generally simulated by the model, although the model slightly underestimated the TC frequency in the western North Pacific and North Indian Ocean (Table 1). In contrast, the SINTEX-F1 considerably underestimates the TC genesis frequency for all TC basins.

Figure 10 shows a comparison of the horizontal distribution of the climatological annual mean of observed and modeled TC genesis frequency. The horizontal distribution of the cyclogenesis simulated by both of the CGCMs is in general agreement with that observed. In particular, the SINTEX-F2 successfully simulates the frequent TC genesis in the western North Pacific and eastern North Pacific as observed (Figures 10a and 10b). The SINTEX-F2, however, underestimates the South Indian Ocean cyclogenesis, while the SINTEX-F1 simulates well. The unsuccessful reproduction of South Indian cyclogenesis in the SINTEX-F2 may result from the less westward extension of the monsoon westerly in the South Indian Ocean during the austral summer (not shown). The weak westerly may suppress the horizontal shear which is favorable condition for TC genesis.

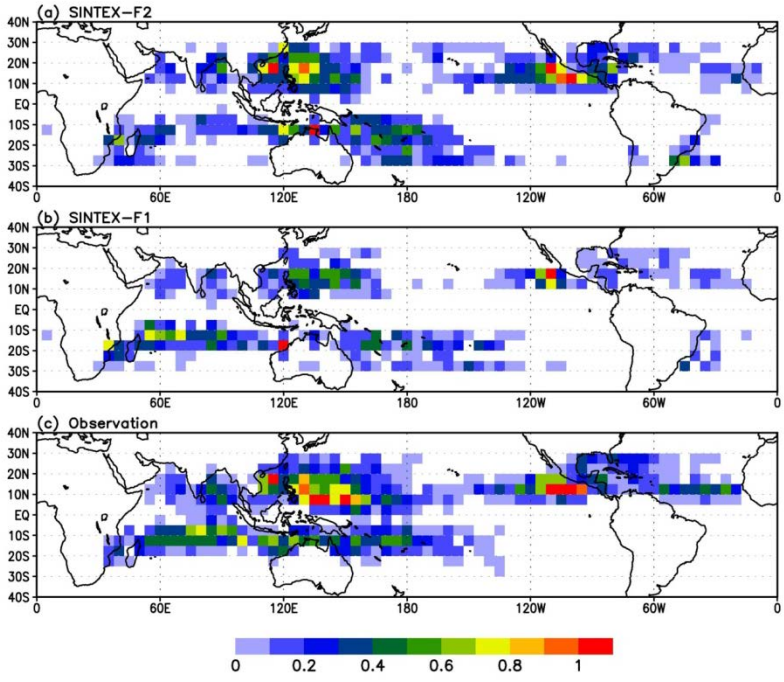

Figure 10. Horizontal distribution of the annual mean of TC genesis frequency from (a) SINTEX-F2, (b) SINTEX-F1, and (c) observation.

Although the SINTEX-F2 well simulates the annual mean of the North Atlantic TC genesis frequency as observed (Table 1), there is a difference in the horizontal distribution of the cyclogenesis between the model and observation. The North Atlantic cyclogenesis is observed primary between 10°N and 20°N (Figure 10c), termed the main development region (MDR; Goldenberg and Shapiro [39]) where African waves propagate westward from Africa across the tropical North Atlantic and Caribbean Sea. The MDR has favorable conditions for the TC genesis: positive low-level relative vorticity (Figure 7c), and weak vertical wind shear (Figure 9c). The SINTEX-F1 and SINTEX-F2 well simulate the high relative vorticity and weak vertical wind shear in the MDR (Figures 7 and 9). However, the modeled TC genesis frequency in the MDR is less than the observed (Figure 9.10). The underestimates of the North Atlantic cyclogenesis frequency is also simulated by the previous medium-resolution CGCM (Fig 17 in [40]). Our results indicate that just increasing the spatial resolution of the CGCM is not enough to improve the location of the North Atlantic cyclogenesis.

Both of CGCMs simulate the TC genesis in the South Atlantic (Figures 10a and 10b), although the cyclogenesis has not been observed in that basin (Figure 10c). The reason for the South Atlantic cyclogenesis in the CGCMs is unclear. The observed South Atlantic SST exceeds 26°C and the vertical wind shear in the basin is relatively weak during the austral summer, while the relative vorticity in the low-troposphere is positive (not shown). This suggests that the anti-cyclonic circulation suppresses the South Atlantic cyclogenesis. The model well simulates not only the warm SST and weak vertical wind shear but also the anti-cyclonic circulation in the South Atlantic. Despite the successful simulation of the South Atlantic large-scale conditions, the model simulates the TC genesis in the basin. The unrealistic South Atlantic cyclogenesis is also simulated by previous medium-resolution CGCMs (Figure 17 in [40]). Further investigation is required to understand this common bias of current models.

Figure 11 shows the seasonal cycle of the TC genesis frequency in the four TC basins in the northern hemisphere. The western North Pacific has a cyclone season during July-October (black line in Figure 11a). The increase in TC genesis during this period is generally reproduced by the two CGCMs (colored lines in Figure 11a). However, there are some discrepancies in the western North Pacific cyclogenesis between the CGCMs and the observations. The SINTEX-F2 overestimates the TC genesis frequency during November-December compared to the observations. In addition, the amplitude of the modeled seasonal cycle of the cyclogenesis is weaker than that of observed. In particular, both of CGCMs underestimate the TC frequency during the peak season (Figure 11a).

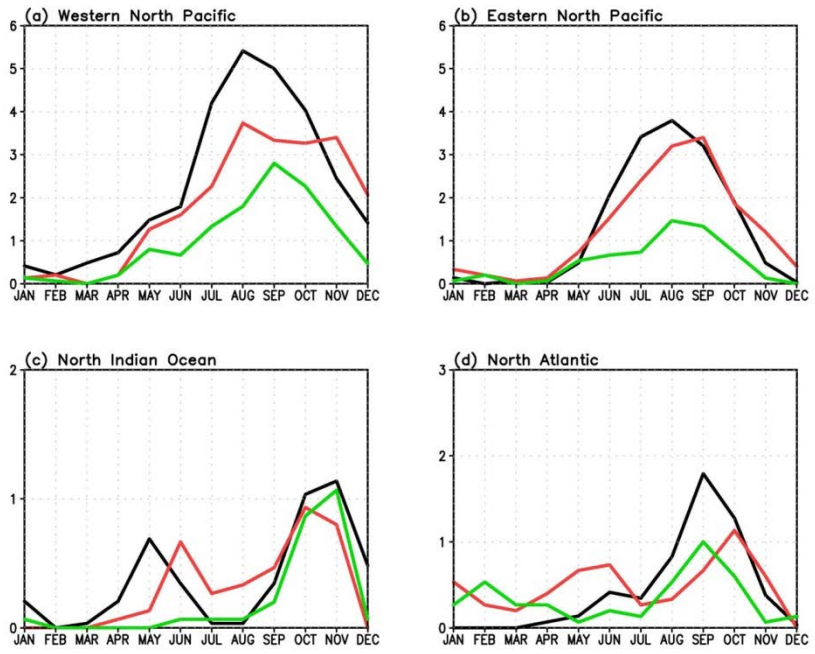

Figure 11. Climatological seasonal cycle of TC genesis frequency over the (a) western North Pacific, (b) eastern North Pacific, (c) North Indian Ocean, and (d) North Atlantic. Black, red, and green denotes the observation, SINTEX-F2, and SINTEX-F1, respectively.

The eastern North Pacific experiences cyclones frequently during boreal summer (black line Figure 11b). The seasonal cycle of the eastern North Pacific cyclogenesis is also well simulated by the two CGCMs, although the amplitude of the modeled seasonal cycle, particularly for the SINTEX-F1, is weaker than the observed.

As shown in Figures 11a and 11b, the seasonal cycle of the TC genesis frequency in the tropical Pacific simulated by the SINTEX-F2 is closer to the observed, compared to that simulated by the SINTEX-F1. In particular, the underestimates of the TC genesis frequency in the SINTEX-F1 are much improved by the SINTX-F2.

The North Indian Ocean has two TC genesis peaks during the pre- and post-monsoon periods (black line in Figure 11c). The North Indian cyclogenesis reduces during the monsoon period due to the strong vertical wind shear of the monsoonal circulation [41]. Instead, weaker than TC systems known as monsoon depressions are formed during the monsoon period. The bimodal seasonal cycle of the North Indian cyclogenesis is reproduced by the SINTEX-F2 to some extent: the modeled TC frequency in June is well simulated while that in May is not (Figure 11c). Meanwhile, the SINTEX-F1 fails to simulate the North Indian cyclogenesis during the pre-monsoon period (Figure 11c). In section 6, we further discuss the possible reasons for the North Indian cyclogenesis during the pre-monsoon period from a view point of the large-scale environmental conditions.

Seasonal cycle of the North Atlantic cyclogenesis is qualitatively well simulated by the SINTEX-F1, although the modeled amplitude is weaker than that of observed (Figure 11d). In contrast, the SINTEX-F2 tends to produce the two cyclone seasons in May and September-October (red line in Figure 11d).

6. SEASONAL CYCLE OF ENVIRONMENTAL CONDITIONS

As we have presented in the Section 5, the high-resolution CGCM reproduces the overall feature of the TC climatology in terms of the genesis frequency, horizontal distribution, and seasonal cycle, although there are some discrepancies between the modeled and observed TC climatology. In this section we further validate the seasonal cycle of TC genesis frequency from a viewpoint of the large-scale environmental conditions with a particular focus on the North Indian Ocean and the western North Pacific.

Figure 12c shows the climatological seasonal cycle of the observed SST averaged over the latitudinal band 5˚N-25˚N, together with the observed climatological TC genesis frequency summed up over the same latitudinal band. As Gray [33] revealed, most of observed TCs are generated over the region where the SST exceeds 26˚C. Both of CGCMs successfully simulates TC genesis over the region where the SST exceeding 26˚C (Figures 12a and 12b).

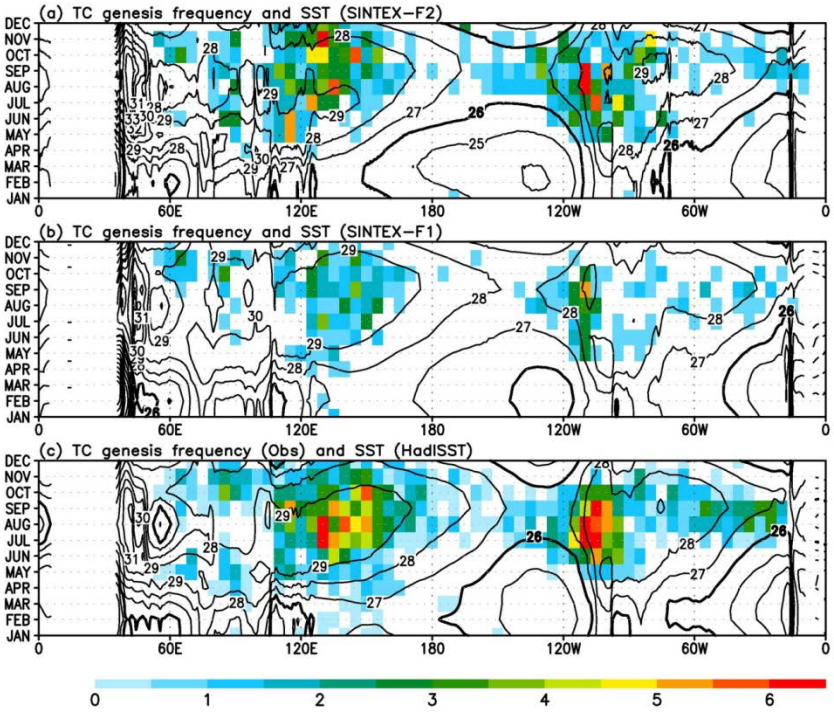

Figure 12. Seasonal cycle of the climatological TC genesis (×10; color) summed up over the latitudinal band 5˚N-25˚N, and SST (contour; °C) from the (a) HadISST, (b) SINTEX-F2, and (c) SINTEX-F1. TC genesis frequency for (a) is calculated from the observed TC data of the NHC and JTWC. Bold line denotes the 26°C isotherm.

A significant difference between modeled and observed seasonal cycle of the North Indian Ocean TC genesis frequency is the less modeled cyclogenesis during the pre-monsoon period (Figure 11c). Furthermore, the SINTEX-F1 simulates no TC genesis in the Arabian Sea and less TC genesis in the Bay of Bengal during the pre-monsoon period compared to that observed (Figure 12b). In contrast, the SINTEX-F2 simulates the TC genesis in the Arabian Sea and Bay of Bengal during the pre-monsoon period (Figure 12a). We however

note that the modeled Arabian cyclogenesis is much less than that observed, while the TC genesis frequency in the Bay of Bengal is greater than that observed (Figures 12a and 12c). These results suggest that the bimodal seasonal cycle of the North Indian Ocean cyclogenesis in the SINTEX-F2 (Figure 11c) results from the unrealistic increase in the TC genesis in the Bay of Bengal during the pre-monsoon period.

The Arabian cyclogenesis in the SINTEX-F2 appears to lag behind by one month compared to that observed (Figures 12a and 12c). Evan and Camargo [41] showed that an early monsoon onset favors Arabian storms in May, while late monsoon onset is typically associated with June storms. This suggests that the less early monsoon onset in the model may suppress the modeled Arabian TC genesis in May.

Gray [42] identified the bimodal seasonal cycle of the cyclogenesis frequency in the Arabian Sea, and attributed the depression of the cyclogenesis in July and August to strong vertical wind shear. The contour in Figure 13c shows the seasonal cycle of the observed vertical wind shear averaged over the latitudinal band 5˚N-25˚N. The vertical wind shear over the Arabian Sea and Bay of Bengal is relatively weak during the pre- and post-monsoon periods (less than 15 ms^{-1}). On the other hand, the vertical wind shear is strong during the monsoon period (Figure 13c). The observed data clearly show that the bimodal seasonal cycle of the Arabian cyclogenesis during the pre- and post-monsoon periods coincides with the periods of the weak vertical wind shear over the Arabian Sea (Figure 13c). The SINTEX-F2 and SINTEX-F1 successfully reproduce the bimodal seasonal cycle of the vertical wind shear in the Arabian Sea, while the modeled Arabian cyclogenesis during the pre-monsoon period is less than that observed (Figure 13). The SINTEX-F2 simulates a few Arabian TCs (Figure 13a), while no Arabian cyclogenesis during the pre-monsoon period is simulated in the SINTEX-F1 (Figure 13b). These results suggest that the vertical wind shear does not explain the less Arabian cyclogenesis during the pre-monsoon period in the CGCMs.

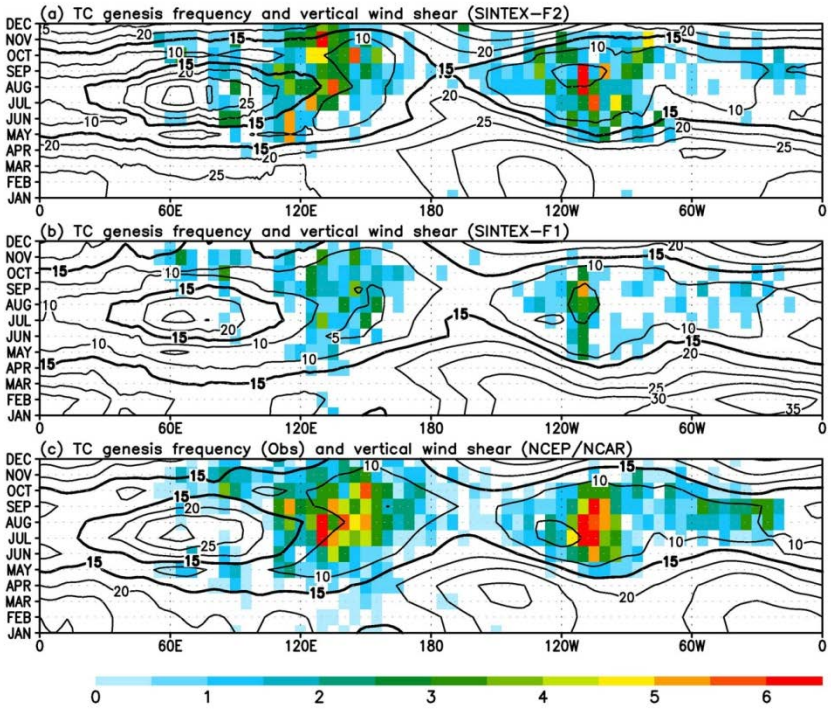

Figure 13. As in Figure 12, but for the vertical wind shear (contour; ms^{-1}) calculated as the difference in the wind speed between the 850- and 200-hPa levels averaged over the latitudinal band 5˚N-25˚N from the (a) NCEP/NCAR reanalysis, (b) SINTEX-F2 and (c) SINTEX-F1. Bold line denotes the 10 ms^{-1}.

The low-level cyclonic circulation is also related to the Arabian cyclogenesis activity. Color shade in Figure 14a shows the climatological seasonal cycle of the observed relative vorticity at the 850-hPa level averaged over the latitudinal band 5˚-25˚N. In the Arabian Sea, there is a good agreement with the increase in observed TC genesis frequency and the enhanced low-level cyclonic circulation (Figure 14c). In contrast, the positive vorticity during the pre-monsoon period in the SINTEX-F2 is ambiguous, while during the post-monsoon period it is significant (Figure 14a). Figure 15 shows the seasonal cycle of the modeled and observed relative vorticity at the 850-hPa level in the Arabian Sea. The relative vorticity from the observation and SINTEX-F2 has the bimodal peaks in the pre- and post-monsoon periods (Figures 15a and 15c). The less Arabian TC genesis during the pre-monsoon period in the SINTEX-F2 may result from the weak positive low-level vorticity in the basin. In case of SINTEX-F1, there is no significant positive vorticity during the pre-monsoon period (Figure 15b). No Arabian cyclogenesis during the pre-monsoon period in the SINTEX-F1 agrees with the low-level anti-cyclonic circulation in the Arabian Sea during this period.

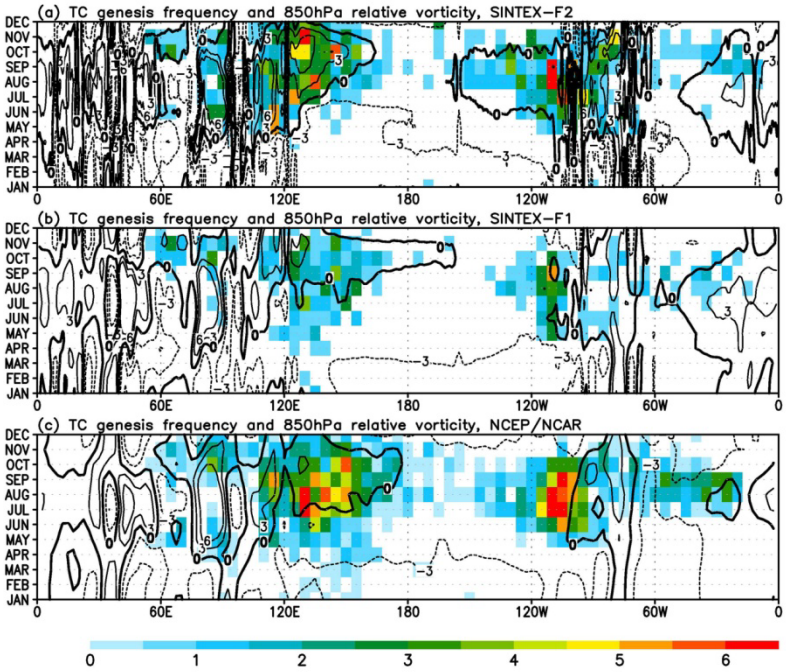

Figure 14. as in Figure 12, but for the relative vorticity at the 850-hPa level ($\times 10^{-6}$ s^{-1}; contour) from the (a) NCEP/NCAR reanalysis, (b) SINTEX-F2 and (c) SINTEX-F1. Bold denotes the zero line.

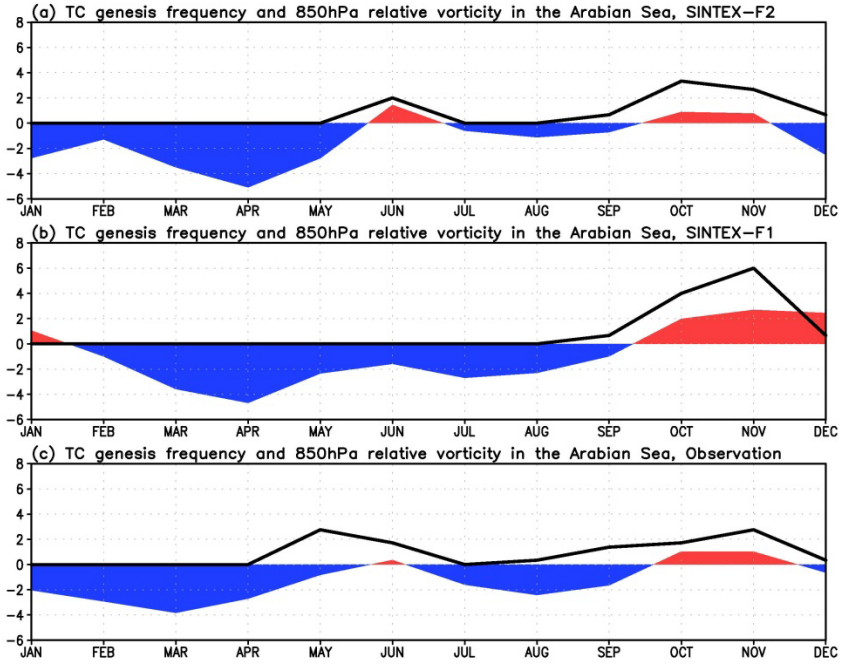

Figure 15. Climatological annual cycle of TC genesis frequency ($\times 10$; black line) and the relative vorticity ($\times 10^6$ s^{-1}; color) at the 850-hPa level over the Arabian Sea from the (a)SINTEX-F2, (b) SINTEX-F1, and (c)observations. Red and blue denote the positive and negative relative vorticity, respectively.

For the western North Pacific, although the high-resolution CGCM well simulates the climatology of TC genesis, the modeled TC genesis frequency is underestimated (Table 1). In addition, if looking carefully, it turns out that modeled TC genesis locations are too much confined to east of the Philippines compared to the observations (Figure 12). Observed data shows that the western North Pacific cyclogenesis locations extend eastward up to the international dateline during the peak season (Figure 12c). During the same period, the monsoon-trough characterized by the weak vertical wind shear and low-level cyclonic circulation also expands eastward to the dateline during the peak season (Figures 13c and 14c). The eastward extension of the weak vertical wind shear is generally simulated by both of the CGCMs. However, the SINTEX-F1 simulates the unrealistic eastward extension of the positive low-level vorticity zone during the boreal autumn (Figure 14b). The unrealistic eastward extension of the positive vorticity zone during boreal autumn simulated by the SINTEX-F1 is improved by the SINTEX-F2. The SINTEX-F2 successfully simulates the eastward extensions of the weak vertical wind shear and low-level cyclonic circulation (Figures 13a and 14a). However, the SINTEX-F2 fails to simulate the eastward extension of

the monsoon-trough up to the international dateline, compared to that of the observed. In particular, observed positive vorticity extends to the large portion of the western North Pacific during July-October, while the modeled positive vorticity zone does not extend as far east as the observed (Figures 14a and 14c). The modeled weak vertical wind shear also does not extend as far east as the observed during the TC peak season compared to that of the observed (Figures 13a and 13c). Thus, the less eastward extensions of the low-level cyclonic circulation and the weak vertical wind shear in the SINTEX-F2 lead to the less TC genesis west of the dateline. The less modeled TC genesis in the southeastern part of the western North Pacific may lead to the less western North Pacific TC genesis frequency (Figure 10).

Figure 14 shows that the observed low-level cyclonic circulation in the western North Pacific extends eastward rapidly in July, while the rapid eastward extension of the cyclonic circulation is not well simulated by the both of CGCMs. The rapid eastward extension of the low-level cyclonic circulation may be related to a rapid increase in the western North Pacific cyclogenesis in July (black line in Figure 11a).

7. TC INTENSITY

Bengtsson et al. [9] showed that higher horizontal resolution AGCM simulates more frequent occurrence of intense TCs. In this section we compare the frequency distribution of the simulated TC surface wind speed between the SINTEX-F2 and SINTEX-F1.

Figure 16 shows a comparison of the modeled and observed frequency distribution of TC surface wind speed in the four TC basins. Over all the TC basins, the TC wind speed simulated by the SINTEX-F1 is less than 20~30 ms^{-1}, while that simulated by the SINTEX-F2 exceeds 30~40 ms^{-1}. The frequency of high wind speed (> 20 ms^{-1}) simulated by the SINTEX-F2 is much greater than that simulated by the SINTEX-F1, while the frequency of the low wind speed (< 15 ms^{-1}) of the SINTEX-F2 is less than that of the SINTEX-F1. As a result, the frequency distribution of TC surface wind speed simulated by the high-resolution CGCM is closer to that of observation compared to the medium-resolution CGCM.

However, the modeled TC intensity even with the high resolution (about 40 km atmosphere) is far from the success. The modeled TC wind speed is less than ~40 ms^{-1}, while the observed one exceeds 60 ms^{-1} (Figure 16). In particular, the difference in the modeled and observed wind speed is large at the mature stage of the TCs. In fact, there is a large difference in the surface wind speed at the latitudinal band of 10˚N-30˚N where TCs develop at its mature stage (not shown). There may be several reasons for the weak TCs in the model compared to those observed. The observed surface wind speed is the maximum surface wind speed for 10 minutes at 6-hour interval, while the modeled surface wind speed is the 6-hour average of the surface wind speed. This suggests that modeled surface wind speed may be reasonably underestimated due to the time-average compared to the observed maximum values. Besides, the model analysis period (15-yr) may be too short to exactly compare with the 29-yr observed TC data. However, the most important factor for the underestimated TC intensity could be due to the model resolution. The horizontal resolution of the SINTEX-F2 (T319) is still too coarse to resolve the inner structure of TCs; the spatial average of surface wind at model grid box may also reduce the simulated TC wind, compared to point-measurement of the observed.

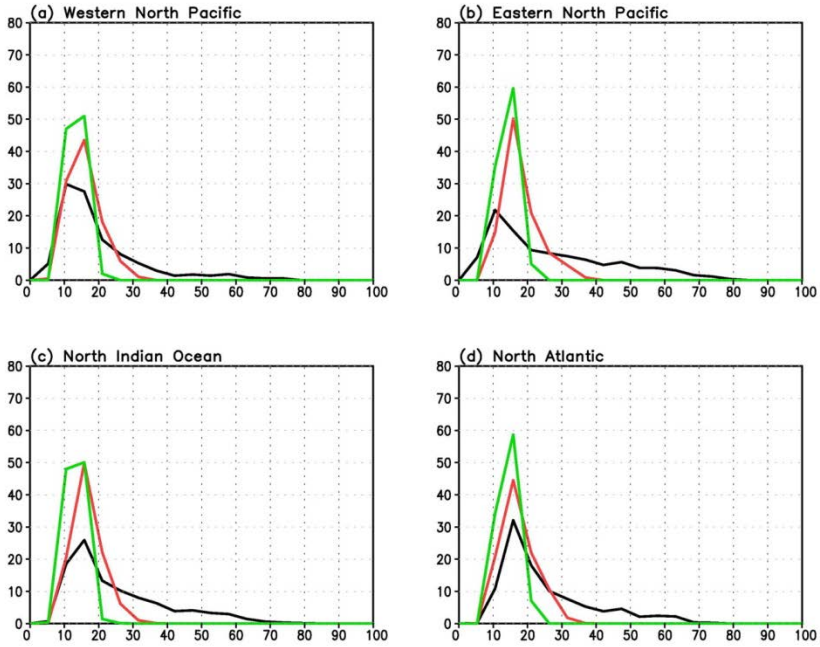

Red and green denote the SINTEX-F2 and SINTEX-F1, respectively. Black shows the observation.

Figure 16. Normalized frequency distribution of modeled and observed surface wind speed of TCs. The unit for the vertical and horizontal axis is % and ms^{-1}, respectively.

SUMMARY AND DISCUSSION

We have examined the global high-resolution CGCM consisting of the T319 AGCM and eddy-permitted OGCM in terms of the climatological TC activity as well as the large-scale environmental conditions favorable for the TC genesis. The overall feature of the climatological TC genesis frequency as well as the environmental conditions is reasonably reproduced by the CGCM. The global TC genesis frequency simulated by the high-resolution CGCM is much closer to the observed, compared that simulated by the medium-resolution (T106) CGCM. In addition, the high-resolution CGCM partially reproduces the bimodal seasonal cycle of the North Indian Ocean cyclogenesis, while the medium-resolution CGCM fails to simulate it. There are, however, still some discrepancies between the modeled and observed TC activity. For instance, although the high-resolution CGCM partially reproduced the bimodal seasonal cycle of the North Indian Ocean cyclogenesis, the model failed to reproduce the Arabian cyclogenesis during the pre-monsoon period. The western North Pacific TC genesis locations are found to be confined in the southwestern sub-domain of the western North Pacific. We discussed the cause of the discrepancy from the view point of the environmental conditions. It has been found that the low-level cyclonic circulation in the

Arabian Sea during the pre-monsoon period is relatively weak compared to that observed, although the vertical wind shear is well simulated as observed. For the western North Pacific, we have found that the modeled monsoon-trough associated with the low-level cyclonic circulation and weak vertical wind shear does not extend eastward far enough compared to that observed. These results suggest that the better reproduction of the large-scale conditions is indispensable for the successful simulation of TC activity. The TC activity can also be simulated reasonably well by the medium-resolution model. Compared to the coarse-resolution model, one of the advantages of the high-resolution CGCM is the reproduction of the intense TC. Surface wind speed exceeding 30~40 ms^{-1} is successfully simulated by the high-resolution CGCM, while the TC wind speed simulated by the medium-resolution CGCM is less than 20~30 ms^{-1}.

We again note that a 5-yr model spin-up for the SINTEX-F2 is insufficient to reach the equilibrium states. Further integration should be needed for the complete simulation and analysis.

Further realistic simulations of TC intensity should be necessary for both the better reproduction of the mean-state of climate and societal applications. Fedorov et al. [43] showed that enhanced vertical mixing associated with enhanced TC activity leads to mix the subsurface ocean waters in the extra-tropical Pacific and thereby increase the temperature of subsurface waters that have been subducted off the coast of California and Chile. This eventually leads to a warming of the Pacific cold tongue SST which in turn enhances TC activity in the region. This ocean-TC feedback hypothesis indicates that the realistic simulation of TC intensity may change the climate conditions as well as TC activity in CGCMs.

Bengtsson et al. [9] showed more frequent intense TC would occur under the global warming condition. Correctly reproducing the TC strength with higher-resolution CGCM would be beneficial to not only TC simulation but also the societal application. Previous studies identified that the U.S. societal damage by a hurricane is proportional to the 3^{rd}-9^{th} power of wind speed at landfall [44]. Although there is uncertainty about how changes in wind speed are related to corresponding changes in the societal damage, the societal damage is no doubt sensitive to the TC intensity. The correct estimation of the TC intensity will be required to make a quantitative assessment of societal damage from TCs, particularly for the assessments of relatively long-term (seasonal-decadal-century timescale) climate impact on society.

REFERENCES

[1] R. A. Madden, P. R. Julian, *Mon. Wea. Rev.*, 122, 814 (1994).
[2] J. C. L. Chan, *Mon. Wea. Rev.*, 113, 599 (1985).
[3] H.-M. Kim, P. J. Webster and J. A. Curry, *Science*, 325, 77 (2009).
[4] H.-M. Kim, P. J. Webster, and J. A. Curry, *J. Climate*, 24, 1839 (2011).
[5] J. P. Kossin and D. J. Vimont, *Bull. Amer. Meteor. Soc.*, 88, 1767 (2007).
[6] J. W. Hurrell, *Science*, 269, 676 (1995).
[7] O. P. Singh, *Current Science*, 94, 29 (2008).

[8] K. Oouchi, J. Yoshimura, H. Yoshimura, R. Mizuta, S. Kusunoki, and A. Noda, *J. Meteorol. Soc. Japan*, 84, 259 (2006).
[9] L. Bengtsson, K. I. Hodges, M. Esch, N. Keenlyside, L. Kornblueh, J.-J. Luo, and T. Yamagata, *Tellus*, 59A, 539 (2007).
[10] M. A. Bender and I. Ginis, *Mon. Wea. Rev.*, 128, 917 (2000).
[11] F. Vitart, and T. N. Stockdale, *Mon. Wea. Rev.*, 129, 2521 (2001).
[12] T. Matsuura, M. Yumoto, and S. Iizuka, *Clim. Dym.*, 21, 105 (2003).
[13] S. Iizuka and T. Matsuura, *Clim. Dyn.*, 30, 815 (2008).
[14] C.-C. Wu, C.-Y. Lee, and I.-I. Lin, *J. Atmos. Sci.*, 64, 3562 (2007).
[15] J.-J. Luo, S. Masson, E. Roeckner, G. Madec, and T. Yamagata, *J. Climate*, 18, 2344 (2005).
[16] E. Roeckner, and Coauthors, "The atmospheric general circulation model ECHAM5, Part I: Model description", Max-Planck-Institut für Meteorologie, Rep. 349, 127 pp (2003).
[17] M. Tiedtke, *Mon. Wea. Rev.*, 117, 1779 (1989).
[18] J. -P. Schulz, L. Dumenil, and J. Polcher, *J. Appl. Meteorol.*, 40, 642 (2001).
[19] G. Madec, NEMO ocean engine, Note du Pole de Modelisation, Institut Pierre-Simon Laplace (2006).
[20] T. Fichefet, M. A. Morales Maqueda, *J. Geophys. Res.*, 102, 12609 (1997).
[21] S. Valcke, A. Caubel, R. Vogelsang, D. Declat, OASIS3 ocean atmosphere sea ice soil user's guide, Technical Report TR/CMGC/04/68, CERFACS, Toulouse, France (2004).
[22] S. Levitus, Climatological atlas of the world ocean, Rep. NOAA Prof. Pap. 13 (1982).
[23] E. Roeckner and Coauthors, "The atmospheric general circulation model ECHAM-4: Model description and simulation of present-day climate", Max-Plank-Institut fur Meteorologie Rep. 218, 90pp (1996).
[24] G. Madec, P. Delecluse, and C. Levy, "OPA 8.1 ocean general circulation model reference manual, LODYC/IPSL Tech. Rep. Note 11, 91pp (1998).
[25] S. Valcke, L. Terray, and A. Piacentini, "The OASIS coupler user guide version 2.4", CERFACS Tech. Rep. TR/CGMC/00-10, 85pp (2000).
[26] E. Kalnay and Coauthors, *Bull. Amer. Meteor. Soc.*, 77, 437 (1996).
[27] N. A. Rayner and Coauthors, *J. Geophys. Res.*, 108, D14, 4407 (2003).
[28] K. J. E. Walsh, M. Fiorino, C. W. Landsea, K. L. Mcinnes, *J. Climate*, 20, 2307 (2007).
[29] W. M. Frank, *Mon. Wea. Rev.*, 105, 1119 (1977).
[30] J. F. Price, *J. Phys. Oceanogr.*, 11, 153 (1981).
[31] M. A. Bender, I. Ginis, and Y. Kurihara, *J. Geophys. Res.*, 98, 23245 (1993).
[32] T. Dickey and Coauthors, *Mon. Wea. Rev.*, 126, 1195 (1998).
[33] W. M. Gray, "Tropical cyclone genesis", Department of Atmospheric Science paper no. 234, Colorado State University, Fort Collins, CO, 121pp (1975).
[34] W. M. Gray, *J. Meteorol. Soc. Japan*, 55, 465 (1977).
[35] J.-L. Lin, *J. Climate*, 20, 4497 (2007).
[36] P. A. Harr, and R. L. Elsberry, *Mon. Wea. Rev.*, 123, 1225 (1995).
[37] K. E. Trenberth, and C. J. Guillemot, *Clim. Dyn.*, 14, 213 (1998).
[38] H. Annamalai, J. M. Slingo, K. R. Sperber, and K. Hodges, *Mon. Wea. Rev.*, 127, 1157 (1999).
[39] S. B. Goldenberg and L. J. Shapiro, *J. Climate.*, 9, 1169 (1996).
[40] S. Yokoi, Y. Takayabu, and J. C. L. Chan, *Clim. Dyn.*, 33, 665 (2009).

[41] A. T. Evan, and S. J. Camargo, *J. Climate*, 24, 140 (2011).
[42] W. M. Gray, *Mon. Wea. Rev.*, 135, 3990 (2007).
[43] A. V. Fedorov, C. M. Brierlrey, and K. Emanuel, *Nature*, 463, 1066 (2009).
[44] R. A. Pielke Jr., *Phil. Trans. R. Soc. A*, 365, 2717 (2007).